

PAPER • OPEN ACCESS

Effects of fast x-ray cone-beam tomographic measurement on dimensional metrology

To cite this article: Charalambos Rossides et al 2022 Metrologia 59 044003

View the <u>article online</u> for updates and enhancements.

You may also like

- Internal surface roughness measurement of metal additively manufactured samples via x-ray CT: the influence of surrounding

material thickness
Joseph John Lifton, Yuchan Liu, Zheng Jie Tan et al.

- Methodologies for model parameterization of virtual CTs for measurement uncertainty

estimation Felix Binder, Benjamin A Bircher, René Laquai et al.

- Electron-optical in-situ metrology for electron beam powder bed fusion: calibration and validation
Christopher Arnold and Carolin Körner

Metrologia 59 (2022) 044003 (11pp)

Effects of fast x-ray cone-beam tomographic measurement on dimensional metrology

Charalambos Rossides¹, Hossein Towsyfyan², Ander Biguri³, Hans Deyhle⁴, Reuben Lindroos⁵, Mark Mavrogordato¹, Richard Boardman¹, Wenjuan Sun⁶ and Thomas Blumensath^{1,2,*}

- ¹ μ-VIS X-Ray Imaging Centre, University of Southampton, Southampton, SO17 1BJ, United Kingdom
- ² Institute of Sound and Vibration Research, University of Southampton, Southampton, SO17 1BJ, United Kingdom
- ³ Department of Applied Mathematics and Theoretical Physics, University of Cambridge, CB3 0WA, United Kingdom
- ⁴ Diamond Light Source Ltd, Harwell Science and Innovation Campus, Didcot, OX11 0DE, United Kingdom
- Department of Computer Science, The University of Bath, Bath, BA2 7AY, United Kingdom
- ⁶ National Physical Laboratory, Hampton Road, Teddington, TW11 0LW, United Kingdom

E-mail: thomas.blumensath@soton.ac.uk

Received 28 April 2022, revised 1 June 2022 Accepted for publication 15 June 2022 Published 12 July 2022



Abstract

X-ray computed tomography (XCT) is increasingly used for dimensional metrology, where it can offer accurate measurements of internal features that are not accessible with other techniques. However, XCT scanning can be relatively slow, which often prevents routine uptake for many applications. This paper explores the feasibility of improving the speed of XCT measurements while maintaining the quality of the dimensional measurements derived from reconstructed volumes. In particular, we compare two approaches to fast XCT acquisition, the use of fewer XCT projections as well as the use of shortened x-ray exposure times for each projection. The study shows that the additional Poisson noise produced by reducing the exposure for each projection has significantly less impact on dimensional measurements compared to the artefacts associated with strategies that take fewer projection images, leading to about half the measurement error variability. Advanced reconstruction algorithms such as the conjugate gradient least squares method or total variation constrained approaches, are shown to allow further improvements in measurement speed, though this can come at the cost of increased measurement bias (e.g. 2.8% increase in relative error in one example) and variance (e.g. 25% in the same example).

Keywords: x-ray tomography, dimensional metrology, conjugate gradient least squares, total variation constraints, iterative reconstruction

(Some figures may appear in colour only in the online journal)

1. Introduction

Coordinate measuring machines (CMM), which are typically used in dimensional measurement, physically drag a contact

Original content from this work may be used under the terms of the Creative Commons Attribution 4.0 licence. Any further distribution of this work must maintain attribution to the author(s) and the title of the work, journal citation and DOI.

probe across the surface [1, 2]. These measurements can thus be greatly affected by the texture of the surface (the mechanical filtering effect), which can be an issue in additive manufacturing [3], where the structure itself might be distorted through a combination of different contact mechanisms [4, 5]. Tactile and optical techniques furthermore do not allow the characterization of internal structures found in many complex additive manufacturing geometries if these do not permit line-of-sight access [3].

^{*} Author to whom any correspondence should be addressed.

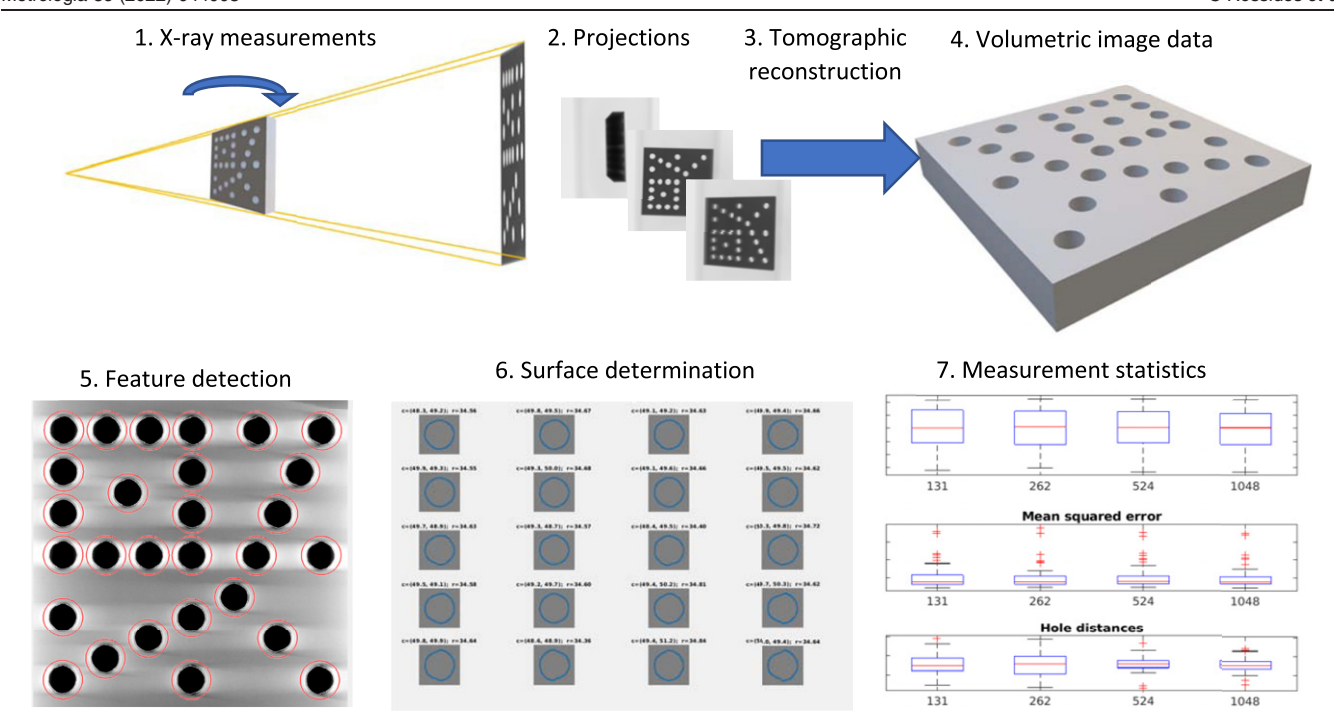


Figure 1. Workflow for the XCT metrology process.

Over the past few years, x-ray computed tomography (XCT) [6] has emerged as an attractive alternative to tactile or optical CMM and has increasingly been used in a broad range of applications in manufacturing and production engineering [7, 8], additive manufacturing process [9, 10] or production integrated inspection of components [11-13]. It has been demonstrated that XCT is able to produce results comparable to those of CMMs and optical inspection systems [2, 14, 15], even though it can still suffer from several sources of measurement error [16, 17]. XCT metrology and quality control [8, 18, 19] has nevertheless undergone a paradigm shift towards holistic, high-resolution measurements applicable to in-line manufacturing applications where it offers several advantages, including non-destructive evaluation of both internal (e.g. non-accessible features [20]) as well as external geometrical features and surface texture characterization with micrometre accuracy [21, 22]. XCT has furthermore the potential to verify parts in assembled states, allowing the detection of manufacturing and assembly induced imperfections, provides simultaneous dimensional and material quality control, and provides complete and high-density point clouds in a relatively short time, all of which are typically not provided by other measurement methods.

To estimate feature dimensions using XCT, several steps are required: tomographic scanning; volumetric image reconstruction [23]; image segmentation [24]; surface determination [25] and dimensional evaluation [16]. This workflow is summarised in figure 1.

Image reconstruction in cone beam CT (the most common form of XCT in industrial settings) is typically done using the Feldkamp, Davis, Kress (FDK) algorithm [23], which is relatively fast and works well in settings where we have enough x-ray transmission through the object (and thus low

Poisson noise in each projection) and where we can collect x-ray projections at sufficiently closely spaced angles to satisfy the tomographic sampling theorem [26]. For reconstruction with higher levels of Poisson noise or from limited projections, iterative optimisation methods are often suggested [27, 28]. These methods are significantly slower than FDK reconstruction, which significantly increases computer hardware requirements as well as reconstruction time. Recent advances in specialised GPU accelerated XCT reconstruction software now enable the use of these techniques also for cone-beam tomographic reconstruction of three dimensional images of realistic size [29], though reconstruction of large volumes can still take several hours [29], restricting their use for inline inspection. Iterative optimisation methods include the conjugate gradient least squares algorithm (CGLS) [30–32], which optimises a least squares objective, though due to ill-conditioning of the XCT inverse problem, regularised methods, such as the fast iterative shrinkage/thresholding algorithm (FISTA) [33] are often preferable. While different approaches to regularisation have been suggested (including early stopping of the CGLS algorithm, which provides implicit regularisation), image smoothness assumptions such as those enforced by the total variation constraint [34] are often preferred, as they provide explicit specification and control of image smoothness conditions.

Once the XCT volumetric image has been reconstructed, dimensional information can be extracted by the determination of object boundaries. Surface determination is realised by various techniques such as assigning or estimating an optimal threshold grey value for edge voxels [25, 35, 36], or interpolation between voxel grey values [37]. Often, parametric curves are then fitted to describe the boundary surface. Once

a surface description is parameterised, dimensional measurements can be obtained in conjunction with calibration data [2, 38]. Despite the rapidly increasing number of applications of dimensional CT metrology in industrial settings [7, 8, 39–41], uptake of this technology remains restricted by the relatively slow scan speed, which often makes the routine inspection of components in a production line setting infeasible [19, 42].

There are two standard approaches available to increase scan speed in XCT: (1) reducing the number of projection images acquired [43] and (2) reducing the x-ray exposure time for each image. When reducing the number of projection images, FDK based reconstruction leads to images with significant artefacts, which in turn often prevent accurate surface determination, while decreased exposure times increases image noise and is thus likely to also increase metrological measurement uncertainty.

In this paper we evaluate performance of two different approaches to increase XCT measurement speed for dimensional metrology. We vary the number of projections (sparse data) and the x-ray exposure times (noisy data). We are particularly interested in the degradation of measurement performance in these settings and on the mitigating effects achievable when replacing the standard FDK algorithm with iterative reconstruction algorithms such as the conjugate gradient method (CGLS) and the total variation constrained FISTA algorithm (FISTA-TV).

2. Materials and methods

We designed a set of experiments and simulations to investigate the performance of the three candidate reconstruction algorithms (FDK, CGLS and FISTA-TV) on fast tomographic acquisition data.

As the sample geometry is application dependent, we investigate two extreme cases (i) a sample with cylindrical symmetry that provides consistent beam path length at all radiographic angles, and (ii) a sample with a flat panel geometry that was mounted so that x-ray paths lengths varied greatly at different angles. Both samples were metal, which introduced additional non-linear attenuation effects known as beam hardening, which are often encountered in inspection settings. The samples were scanned twice using our in-house custom built XCT scanner. One slow scan minimised noise and blurring while a fast scan had a much higher noise level.

The low noise (long exposure) scan data was used to generate additional data-sets. By adding additional Poisson noise, data with intermediate noise levels was generated, while by removing a subset of the projection images from the data, limited projection acquisitions were generated. The different data-sets were then reconstructed with the FDK, CGLS and FISTA-TV reconstruction algorithms (see section 2.4). Surfaces were fitted to different structures in each volumetric image from which metrological measurement points could be extracted and compared with dimensional information measured using co-ordinate measurement machines (see section 2.5). As each sample has several features, this gave us a wide range of metrological measurements for each of

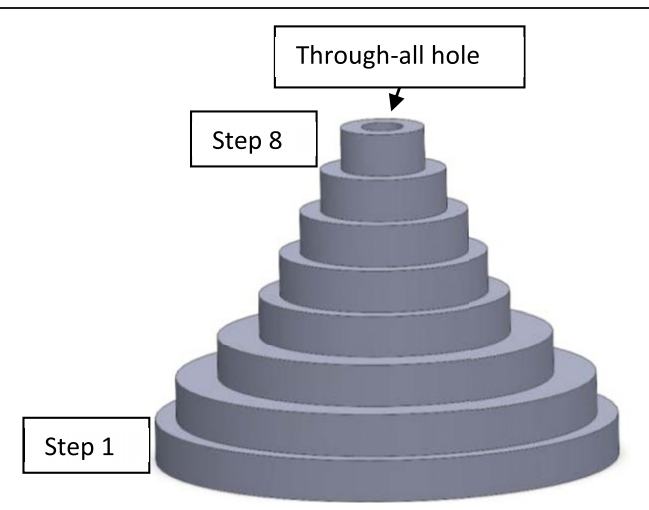


Figure 2. A schematic lay-out of the calibrated cylinder-stack sample. The sample is manufactured out of aluminium and consists of 8 equal height steps. The overall height is 160 mm. The sample also has a 20 mm central through hole. Measured diameters along the centre of each step are given in table 1.

Table 1. The dimensions of the cylinder-stack sample measured with a CMM device.

Feature	Diameter/mm	Cylindricity/mm	
Inside top	20.0145	0.0070	
Step 8	40.0074	0.0059	
Step 7	59.9989	0.0037	
Step 6	79.9922	0.0047	
Step 5	99.9872	0.0039	
Step 4	119.9832	0.0034	
Step 3	159.9824	0.0061	
Step 2	199.9851	0.0084	
Step 1	220.0319	0.0200	
Inside bottom	20.0337	0.0105	

the conditions of interest, while fixing many of the aspects of the experiment (such as sample shape and material) that are also known to influence metrological performance, but whose variation would here hide the influence of the different imaging approaches and reconstruction algorithms on measurement accuracy and precision.

2.1. Sample designs and dimensions

The step-cylinder and CMM reference measurements were provided by the Swiss Federal Laboratories for Materials Science and Technology (EMPA) [44]. This 160 mm height aluminium sample features 8 concentric cylindrical steps of equal height but with different diameters and a concentric through-all hole as shown in figure 2 and table 1.

The hole-plate sample (shone diagrammatically in figure 3) was manufactured and calibrated by the Physikalisch-Technische Bundesanstalt (PTB) [45] (sample number 'PTB 3' in [45]).

The sample is a stainless-steel plate measuring ($6 \times 6 \times 1$) mm with 28 holes with nominal diameter of 0.5 mm. The exact dimensions of the sample we use here were quantified by PTB and are summarised in table 2.

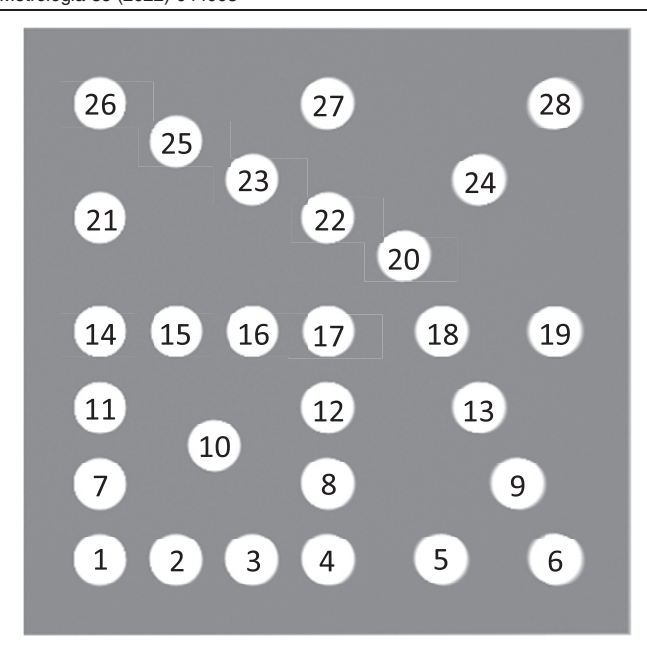


Figure 3. A schematic lay-out of the hole-plate sample.

Table 2. Example dimensions of the hole-plate sample measured with a CMM device (average over three repeat measurements, all measurements were available but are omitted here for compactness).

Hole number	Diameter/mm	Cylindricity/mm	
1	0.5043	0.000 589	
2	0.5041	0.000776	
7	0.5042	0.000782	
8	0.5043	0.000 598	
11	0.5044	0.000772	
13	0.5040	0.001 212	
16	0.5040	0.000707	
17	0.5040	0.000 935	
24	0.5041	0.000798	
26	0.5044	0.000764	
28	0.5038	0.000697	

2.2. X-ray CT scanner

All scans were carried out at the $\mu\textsc{-VIS}$ X-Ray Imaging Centre at the University of Southampton, Southampton, United Kingdom. A Nikon/X-tek systems Ltd custom-built x-ray CT scanner was used to perform the experiments. Image acquisition and overall control of the system was performed with the Nikon/X-tek systems Ltd Inspect-X software (Inspect-X v2). A Nikon 450 kV micro-focus x-ray tube was used as a source, with a tungsten (W) reflection target for the step cylinder, while a Nikon 225 kV source was used for the hole plate. Both sources allow for exchangeable x-ray filters. The system also features an XYZ sample stage, and a high sensitivity flat panel detector [Perkin Elmer XRD 1621 CN3 EHS, with (2000 \times 2000) pixels of 0.2 mm pixel pitch], movable linearly in three orthogonal directions.

At the detector, an analogue gain, measured in decibels (dB), is used to multiply the recorded signal (photon counts

Table 3. The scan parameters for the slow and fast scan.

	Slow scan	Fast scan	Low projection		
Step cylinder					
CGLS					
Iterations	20	20	20		
FISTA (TV)					
Iterations Hyper TV iteration Lambda	20 220000 20 0.1	75 6000 20 0.1	75 6000 20 0.1		
CGLS					
Iterations	20	20	20		
FISTA (TV)					
Iterations Hyper TV iteration Lambda	20 220000 100 10	20 220000 100 10	20 220000 100 10		

per pixel) to compute the output signal (grey value intensity stored as 16 bit unsigned integers). The system provides the capability of frame averaging, where projection images are taken repeatedly at the same rotation angle, which are then averaged, thus reducing photon counting and thermal noise.

A shuttling feature slightly shifts the detector over the duration of image acquisition with radiographs being co-registered post-imaging, a process that minimises errors originating in mechanical misalignment of the imaging setup. Both methods, frame averaging and shuttling, improve the imaging quality by suppressing imaging errors at the expense of longer scan times. Projection images can be taken either using a stop/start scanning approach, where the manipulator is rotated to a new angle, the motion stopped and only then, a projection image is taken. The alternative is to use a continuous rotation scanning approach, where a continuous rotation is used with images acquired while the object remains in motion. Continuous rotation is much faster, but will introduce increased blurring for longer exposure times or when averaging over more frames.

2.3. CT data acquisition

Two scans were performed for each of the two samples. Scan parameters are given in table 3. One slow, high-quality scan used frame averaging, long exposure times and stop/start scanning, while a fast scan used short exposure times, no frame averaging and a continuous rotation scanning strategy. The slow scan minimised noise while the fast scan minimised overall data acquisition time. Both scans took the same number of projection images to allow standard tomographic reconstruction.

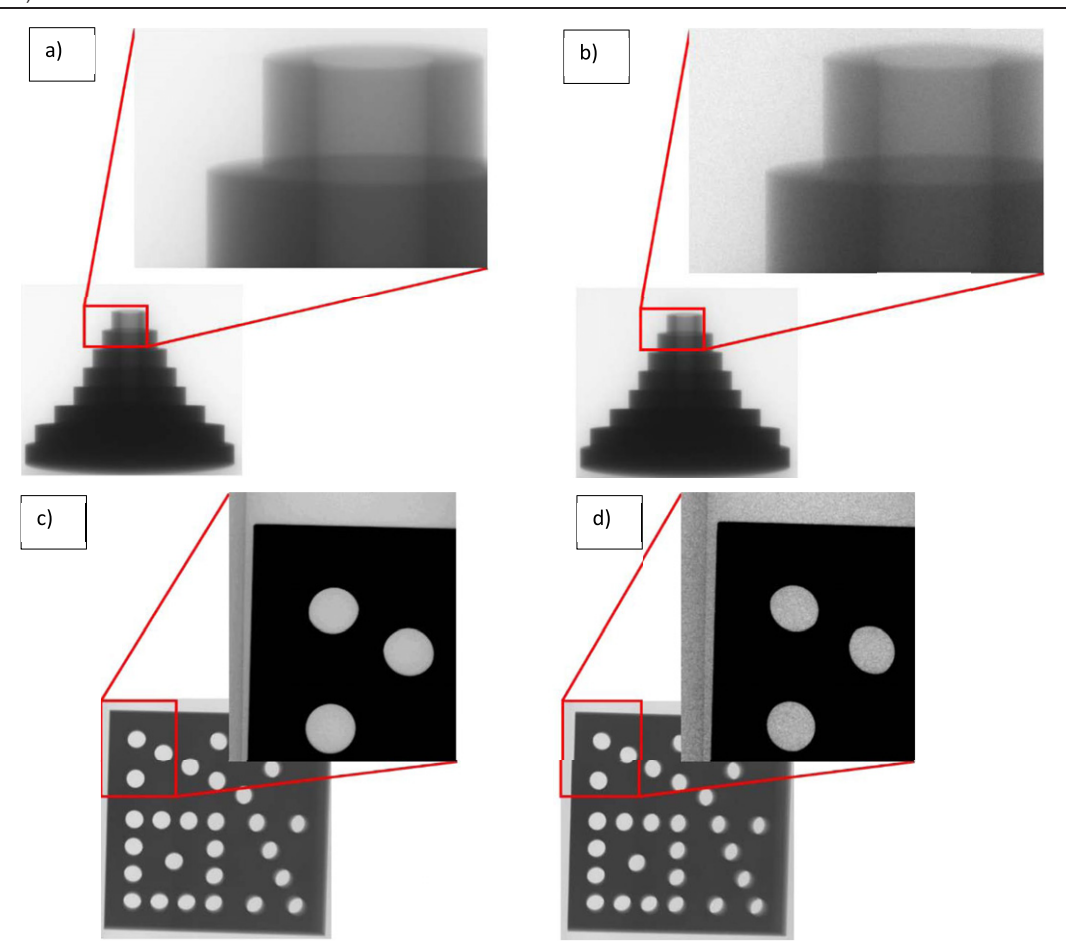


Figure 4. Sample radiographs of the cylinder-stack (a) and (b) and the hole-plate (c) and (d) samples, with a detail in the red box enlarged for better preview. Slow scan radiographs in (a) and (c) comprise higher SNR compared to their fast scan equivalents (b) and (d), respectively.

Table 4. The reconstruction protocols for the slow and fast scans of the step cylinder, for the CGLS algorithm and the FISTA TV algorithm.

	Step cylinder		Hole plate	
Scan speed	Slow	Fast	Slow	Fast
X-ray tube voltage/kV	390	390	120	120
X-ray tube current/mA	0.245	0.216	0.083	0.083
Power/W	95.6	84.2	10	10
Exposure time/ms	708	250	134	134
Frames per projection	16	1	16	1
Number of projections	3143	3143	3143	3143
Filter sheet thickness/mm	8	8	_	_
Filter sheet material	Copper	Copper	_	
Shuttling	Yes	No	Yes	No
Start/stop or continuous	S/S	Cont.	S/S	Cont.
Scan duration/mins	760	13	112	7

For the step cylinder the slow scan took 760 min, while the fast scan took 13 min (58 times faster). For the hole-plate the slow scan took 112 min, while the fast scan took 7 min (16 times faster). The temperature in the CT scanner was recorded as (25 \pm 1) °C. Sample projection images for fast and slow scans are shown in figure 4 for both samples, with magnified image portions showing the image noise. The slow

Table 5. The reconstruction protocols for scans of the hole-plate sample and for increasing number of projections, for the CGLS algorithm and the FISTA TV algorithms.

No. of projections	131	262	524	1028
	CG	LS		
Iterations	75	75	75	75
	FISTA	(TV)		
Iterations	75	75	75	75
Hyper	22	333	955	2200
TV iterations	100	100	100	100
Lambda	0.1	0.1	0.1	0.1

scan was then used to generate an additional dataset by discarding projections, thus simulating another fast scan, where this time few low noise projections are used.

These low projection fast scans used only 54 projections to simulate a scan that, for the step-cylinder, would have been as fast as the high noise scan. These scans were used in a first experiment to compare the effects on dimensional metrology of the different approaches to increase imaging speed and the effects of different reconstruction algorithms on these.

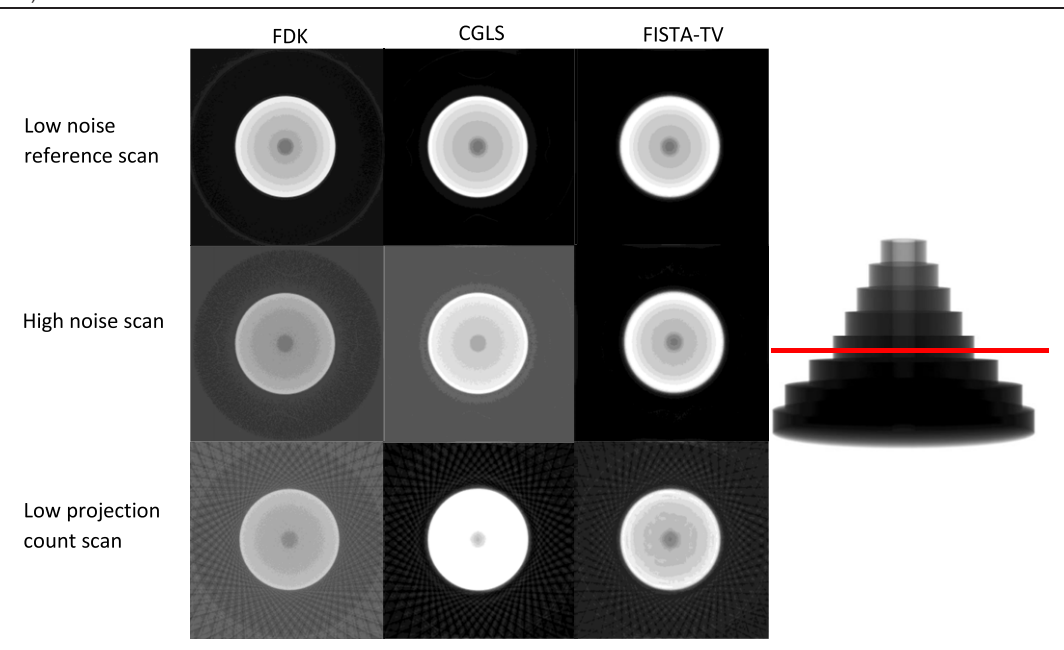


Figure 5. Comparison of scan settings and reconstruction methods in an image slice passing through step 4.

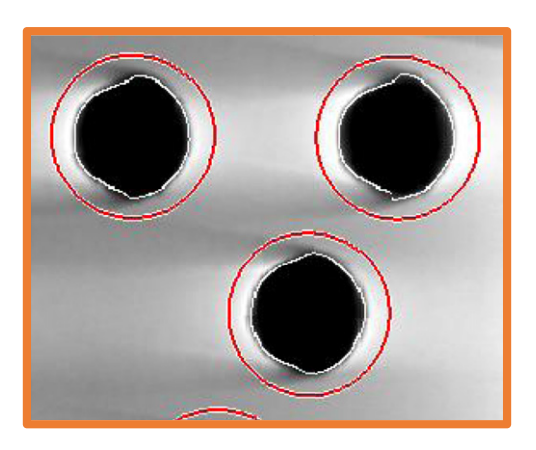


Figure 6. Circles (red) derived using the Huff transform identify the location of each hole. Canny edge detection identifies hole boundaries (white). Circle fitting (not shown) fits circles to identified boundary points.

In a second set of experiments, further simulated scans were produced from the low noise fast scans. The first set of simulated data used the low noise images, but reduced the dataset size to 132, 262, 524 and 1048 equally spaced projections, while a second set of simulated data added Poisson noise to the projections to simulate data that would have been acquired with 1800, 18000 and 90000 photons per pixel along x-ray paths that do not intersect with the object (we also generated data with an average photon count of 180 photons per pixel, but this data did not provide reconstructions that allowed surface fitting).

2.4. Reconstruction

All data-sets (the slow, low noise reference scans, the high noise scans and the low number of projection scans) of the step-cylinder and the hole-plate samples were reconstructed

Table 6. The reconstruction protocols for scans of the hole-plate sample and for increasing Poisson noise variance, for the CGLS and the FISTA TV algorithms.

Photon count	1800	18000	90000
	CGLS	1	
Iterations	75	75	75
	FISTA (T	ΓV)	
Iterations	75	75	75
Hyper	2200	2200	2200
TV iterations	100	100	100
Lambda	0.1	0.1	0.1

using the standard FDK [23, 45] algorithm as implemented in the TIGRE tomographic reconstruction software [29, 46]. This FDK reconstruction was used as the baseline to compare the performance of two iterative methods. The FDK reconstruction of the slow, low noise scans were also used to calibrate the system parameters and to determine the size of the reconstructed voxels to match the average coordinate measurement machine dimensions for both samples. This allowed us to analyse the performance of alternative reconstruction algorithms, such as the CGLS [30–32], and FISTA-TV algorithms [33], both implemented in the TIGRE toolbox [29, 46].

Parameters for the iterative algorithms for the first set of experiments, where we reconstructed the slow, low noise data, the fast, high noise data and the low noise data with only 54 projections are shown in table 4. FISTA-TV algorithm parameters were optimised by running a few iterations of the reconstruction over a grid of parameters and observing image quality. Example reconstruction images are shown in figure 5 where we show slices through the reconstruction volume of the step cylinder sample, dissecting the fourth step from the bottom and figure 6, where we show portion of a slice through

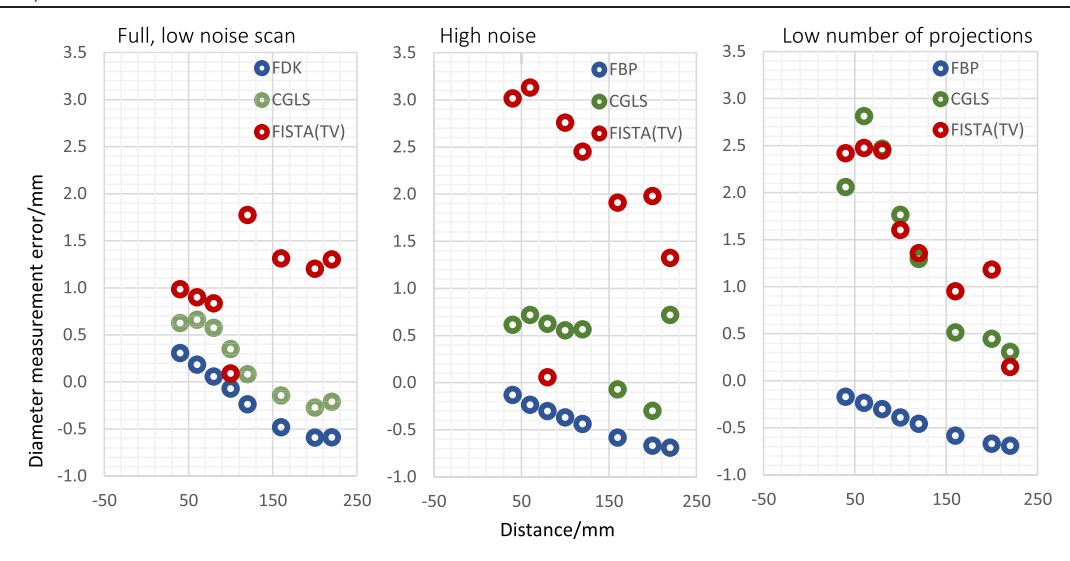


Figure 7. Measurement errors for the measurements of outer diameters measured on the step cylinder from the slow, low noise scan for the FISTA(TV) algorithm, the CGLS algorithm and the FDK algorithm.

the centre of the reconstructed hole plate. The parameters for the iterative algorithms for the second set of experiments, where we reconstructed the 4 data sets with different projection counts and the three datasets with different noise levels, were tuned in a similar way. The parameters are shown in tables 5 and 6.

2.5. Surface determination and measurements

For the first experiment, surface determination was carried out using VG studio 3.4 using the advanced mode iterative surface determination method provided in the VG Metrology package. For the step cylinder, the cylinder axis of the smallest diameter step was used to define a co-ordinate axis (we initially planned to use the internal through hole as axis to define the coordinate system, but beam hardening artefacts prevented the fitting of a cylinder to this feature). We then defined orthogonal planes relative to that axis, where each plane intersected the centre of each cylindrical step. The intersection of the step boundary and the relevant plane defined measurement points to which a circle was fitted. We then measured the root mean square deviation of measurement points from the circle as well as the max/min deviation.

For the hole plate, we again used VG studio 3.4 using the advanced mode iterative surface determination method to fit all surfaces. We used the front surface to define a reference plane. We then fit cylinders to all holes, using holes 1 and 6 to define a coordinate axis by connecting the intersections of the two cylinder central axes and the reference surface. Using the normal to the surface as another axis then provided an orthogonal co-ordinate system for measurement. We measured the diameters of all cylinders as well as centre to centre distances (measured on the reference surface) for cylinder hole pairs (1, 28), (6, 20), (26, 20), (1, 26), (1, 6), (4, 27) and (14, 19).

For all measurements, the CMM data for sample features was then used as a baseline to estimate the systematic error [2] $E = x_{\text{CT}} - x_{\text{ref}}$ and relative errors: $E_r = \frac{x_{\text{CT}} - x_{\text{ref}}}{x_{\text{ref}}}$, where x_{ref} is the reference measurement [47, 48].

For the second set of experiments, we analysed only the data from the hole plate. As it is unclear what procedure VG studio's iterative surface determination approach takes and to verify our results using an alternative approach, Canny edge detection was used to determine object surfaces. The central line between top and bottom surface points was identified and the three dimensional data was resampled along the central slice using bi-cubic interpolation to produce a two dimensional image. The Huff circle finding method was used to locate all holes and generate masks for hole location including both the hole and a margin around the hole. Canny edge detection identified hole boundaries in each masked area (see figure 6). A least squares approach was used to fit a circle to the boundary points of each hole. Circle diameters and hole centre to centre distances were computed for all holes and hole pairs. Looking at figure 6 we also see visible distortion of the detected holes, which were here mainly due to beam hardening artefacts [45] evidence of which can be seen here, which was further verified using the full reconstructed volume (not shown).

3. Results and discussion

Results for the errors in the measurement of outer diameters (step cylinder) with the different algorithms is shown in figure 7, where we show the error in the measured diameters for each method and each of the three datasets plotted against the nominal diameters of each cylinder. It is worth noting that for larger diameters, beam-hardening effects become evident.

Results for the errors in measuring inner diameters (hole plate data) with the different algorithms is shown in figure 8, where we show a box whisker plot for the errors for all holes for any one dataset/algorithm combination.

Figure 9 quantifies the average error as well as the standard deviation of the errors in the hole plate. We here look at the inner diameter error and its variation for 26 all holes as well as the average relative error and its variation for hole centre to centre distances between hole pairs (6-20), (20-26), (4-27), (1-26), (14-19), (1-6) and (1-28). For the outer diameters of

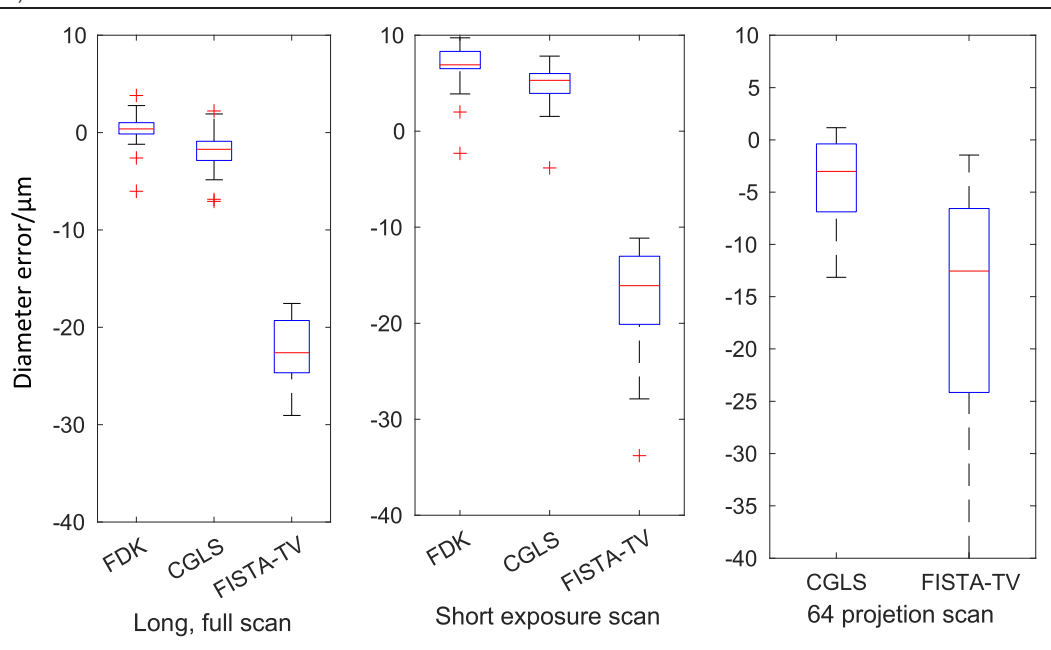


Figure 8. Box and whisker plots of the errors in the hole diameter estimates in μ m for the hole plate for the different measurements [low noise scan (right), high noise scan (middle) and low number of projection scan (right)] for the three different algorithms. Box and whisker plots show the median (red line), interquartile range from 25% to 75% percentile points (blue box), the -3 standard deviations (std) to +3 std from the data mean range (black whiskers) and outliers (red +), i.e., points > 3 std and < -3 std.

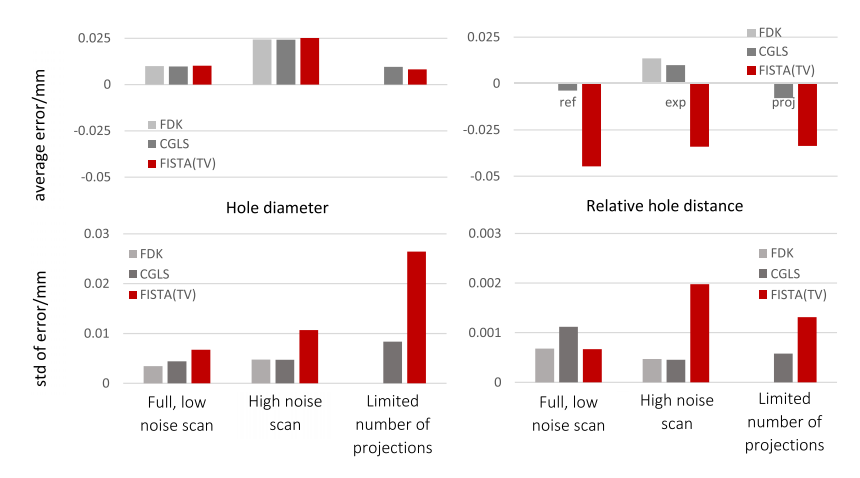


Figure 9. Average (top) and standard deviation (bottom) in the error in the hole diameter (left) and the relative hole centre to centre distance (right) for the three hole plate datasets for all three algorithms. FDK did not provide reliable surface estimates for the limited projection data.

the step cylinder, we see that the error for all methods varies with step diameter and this is here likely to be due to beam hardening effects, with larger steps showing increasing beam hardening issues in the reconstruction due to the highly attenuating material used (aluminium). Another observation is that both, the CGLS and the FISTA method give biased results, with the bias being positive for the outer diameters (outer diameters are overestimated) while the inner diameters lead to negative bias (inner diameters are underestimated). Crucially, the bias is much larger for the FISTA-TV method, indicating that the total variation constraint leads to boundary estimates that are biased towards the outside of the object. Note that this is similar to issues known to be produced in XCT based surface determination, where inner diameters tend to be more sensitive to image noise and artefacts [49] and our results suggests that

this issue is further amplified by the use of the TV constraint in the reconstruction.

Another observation is that the results for the FISTA algorithm show much larger variation compared to the other methods. This is particularly evident for steps 5 and 6 of the phantom, where the FDK reconstruction provides significantly different results for the three data-sets. Note that the FDK algorithm was not able to reconstruct the hole plate low projection count data with sufficient accuracy to allow us to fit the required surfaces, so results for this case are missing here.

To analyse the influence of the surface fitting used and to see the performance of the methods over a wider range of noise levels and reductions in projections, we used the artificially generated noisy scan data and a wider range of the low projection count data as described above. Results are shown in figure 10, where we show the errors in the hole diameter

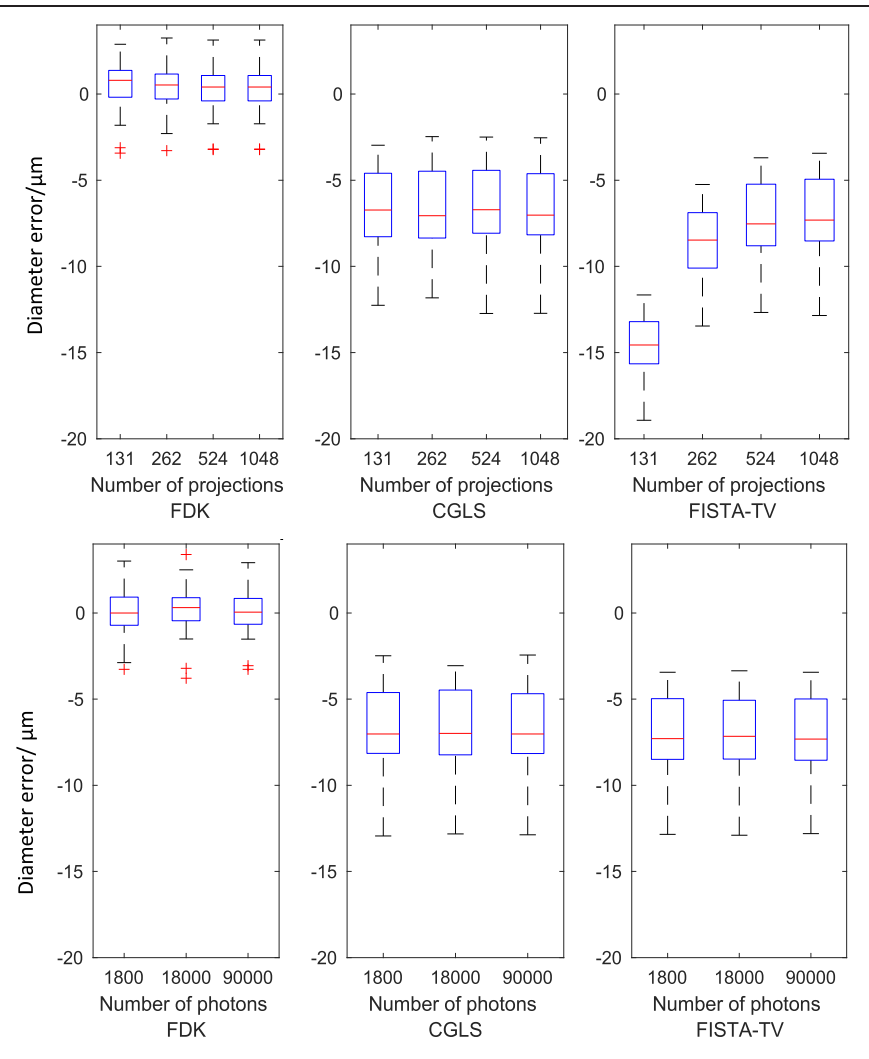


Figure 10. Box and whisker plots of the hole diameter errors (in μ m) measured for the hole plate using limited numbers of x-ray photons (top) and limited numbers of projections (bottom) and reconstructed with the three different algorithms.

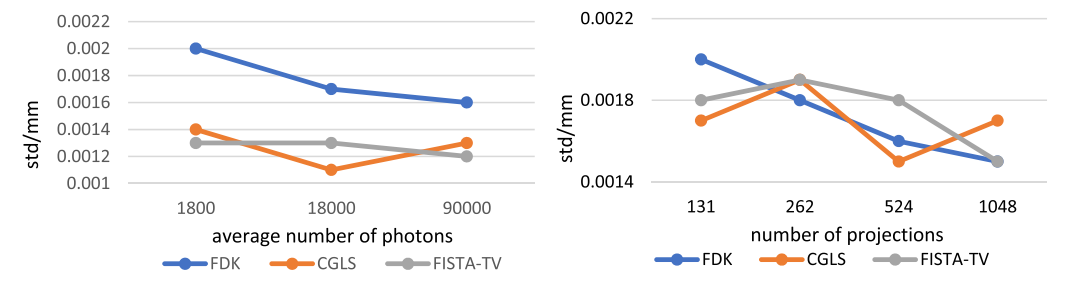


Figure 11. The standard deviation of the normalised distance between through holes on the hole plate in mm plotted for the three algorithms for different numbers of photon counts per pixel (left) and different number of projections (right).

estimates achieved with the different methods. Again, we see that the CGLS method and the FISTA-TV algorithm led to increasingly biased results, with the bias in the FISTA-TV reconstruction getting worse in for the dataset with the smallest numbers of projections, mirroring the results above. The same deterioration is not shown in the FISTA results for the data with the highest noise level. Note, that, when reconstructing the data using a photon count of 180, we did not find reliable edges to use our circle fitting approach. We see that the results for the FISTA algorithm here show smaller errors compared to those found for the results with the low noise data. This indicates

that either, the slightly different FISTA-TV parameter choice used here gives rise to somewhat different results or that the surface determination approach used above is more sensitive to the FISTA-TV bias than the Canny method.

These results suggest that both surface determination methods are relatively robust to the photon counting noise associated with acquisitions with shorter exposure times, while the streaking artefacts introduced when reducing the numbers of projections more quickly deteriorates surface estimates. While the centre-to-centre hole distance measures are more robust than the hole diameter estimates (which is to be expected as

biases in surface estimation here cancel out), looking at the standard deviation of the normalised error in hole to hole distances across the sample shows an increase in distance measure variability for all methods and for both scenarios for the increase of noise and the decrease in the number of projections (figure 11). This change is relatively predictable for the FDK reconstruction, which, for example, shows a near linear decrease in the standard deviation of the normalised distance error for doubling numbers of projection. For CGLS and in particular the FISTA-TV results, this relationship is less clear with results much more variable.

4. Conclusion

We have here shown how a reduction in scan time can be achieved in XCT metrological measurements by decreasing x-ray exposure or by reducing the number of x-ray projections. While iterative algorithms can help with the loss of fidelity, results also become increasingly biased and more variable depending on the type and amount of image degradation induced by the faster imaging strategy.

In particular, we observed that a total variation based reconstruction method biased surfaces to be located further towards the outside of the objects, making inner diameter measures smaller and outer measures larger, a phenomenon previously observed in dimensional XCT, but here shown to be stronger with TV based reconstruction, but also observed, though to a lower extent, for the least squares approach. For example, FISTA-TV reconstruction led to a median relative error in the estimation of inner diameters of -2.8% (with 131 projections, a 24 times speedup) to -1.4% (with 1048 projections, a 3 times speed up) relative to FDK reconstruction. The standard deviation in the error increased by approximately 25% for all of these conditions with FISTA-TV. For 64 projections, the standard deviation in the relative measurement error for FISTA-TV increased from 0.5% to 1.3% though here, FDK reconstruction no longer provided useable surface estimates. Similar, but opposite effects were observed for the outer diameters, with the FISTA-TV reconstruction leading to a median relative error in the estimation of outer diameters of -2.1%(with 64 projections, a 49 times speedup) relative to FDK reconstruction with a standard deviation in the relative error of 2.1% compared to a standard deviation of only 0.03% for the FDK algorithm.

Comparing the decrease in x-ray exposure to the reduction of the number of projections, we observe a doubling in the error standard deviation for the inner diameter measurements when going from the reduced exposure time scans and the limited projection scans for both iterative methods, while the FDK method completely fails for the limited projection data. For the outer diameter, the same trend is observed, though it is here more variable.

Acknowledgments

The authors gratefully acknowledge the support of NVIDIA Corporation with the donation of the Titan Xp GPU used for this research. This research was supported by EPSRC Grant

EP/R002495/1 and the EMPIR Project 17IND08, which has received funding from the EMPIR programme confirmed by the Participating States and from the European Union Horizon 2020 Research and Innovation Programme. The authors acknowledge the μ -VIS X-Ray Imaging Centre at the University of Southampton for the provision of the x-ray tomographic imaging facilities.

ORCID iDs

Charalambos Rossides https://orcid.org/0000-0002-7547-0256

Ander Biguri https://orcid.org/0000-0002-2636-3032

Hans Deyhle https://orcid.org/0000-0002-9095-2069

Mark Mavrogordato https://orcid.org/0000-0002-3956-2866

Richard Boardman https://orcid.org/0000-0002-4008-0098 Wenjuan Sun https://orcid.org/0000-0001-5888-111X Thomas Blumensath https://orcid.org/0000-0002-7489-265X

References

- [1] Puertas I, Pérez C J L, Salcedo D, León J, Luri R and Fuertes J 2013 Precision study of a coordinate measuring machine using several contact probes *Proc. Eng.* 63 547–55
- [2] Villarraga-Gómez H, Lee C and Smith S T 2018 Dimensional metrology with x-ray CT: a comparison with CMM measurements on internal features and compliant structures *Precis*. *Eng.* 51 291–307
- [3] Lou S, Brown S, Sun W, Zeng W, Jiang X and Scott P 2019 An investigation of the mechanical filtering effect of tactile CMM in the measurement of additively manufactured parts Measurement 144 173–82
- [4] Bos E 2011 Aspects of tactile probing on the micro scale *Precis*. Eng. 35 228–40
- [5] Swornowski P 2013 A critical look at the coordinate measuring technique *Mechatronics* 23 80–93
- [6] Villarraga-Gómez H, Herzo E L and Smith S T 2019 X-ray computed tomography: from medical imaging to dimensional metrology *Precis. Eng.* 60 544–69
- [7] De Chiffre L, Carmignato S, Kruth J-P, Schmitt R and Weckenmann A 2014 Industrial applications of computed tomography CIRP Ann 63 655–77
- [8] Villarraga-Gómez H 2016 Seeing is believing: x-ray computed tomography for quality control Quality Magazine, BNP Media 55 93331 https://www.qualitymag.com/articles/93331
- [9] Thompson A, Maskery I and Leach R K 2016 X-ray computed tomography for additive manufacturing: a review *Meas. Sci. Technol.* 27 072001
- [10] Everton S, Hirsch M, Stravroulakis P, Leach R and Clare A 2016 Review of in situ process monitoring and in situ metrology for metal additive manufacturing Mater. Des. 95 431–45
- [11] Stopp J, Christoph R and Christoph R 2018 Productionintegrated metrology with modern coordinate measuring machines using multisensor and x-ray computed tomography systems *The Int. Symp. for Production Research*
- [12] Eberhorn M, Oeckl S, Stocker T and Brunner F 2016 Novel handling concept for production integrated computed tomography World Congress on NDT
- [13] Brunke O, Hansen F, Stuke I, Butz F and Jeltsch F 2013 A new concept for high-speed atline and inline CT for up to

100% mass production process control 16th Int. Congress of Metrology

- [14] Gapinski B, Wieczorowski M, Marciniak-Podsadna L, Dybala B and Ziolkowski G 2014 Comparison of different method of measurement geometry using CMM, optical scanner and computed tomography 3D *Proc. Eng.* 69 255–62
- [15] Carmignato S and Savio E 2011 Traceable volume measurements using coordinate measuring systems CIRP Ann 60 519-22
- [16] Jiménez R, Ontiveros S, Carmignato S and Yagöe J 2012 Correction strategies for the use of a conventional micro-CT cone beam machine for metrology applications *Proc. CIRP* 2 34–7
- [17] Léonard F, Brown S, Withers P, Mummery M P and McCarthy M 2014 A new method of performance verification for x-ray computed tomography measurements *Meas. Sci. Technol.* 25 065401
- [18] Carmignato S, Dewulf W and Leach R 2018 Industrial X-Ray Computed Tomography (Berlin: Springer)
- [19] Kruth J, Bartscher M, Carmignato S, Schmitt R, De Chiffre L and Weckenmann A 2011 Computed tomography for dimensional metrology CIRP Ann 60 821–42
- [20] Xu D, Cheng F, Zhou Y, Matalaray T, Lim P and Zhao L 2019 Process optimization: internal feature measurement for additive-manufacturing parts using x-ray computed tomography Int. Symp. on Precision Engineering Measurements and Instrumentation
- [21] Quinsat Y, Guyon J B and Lartigue C 2019 Qualification of CT data for areal surface texture analysis Int. J. Adv. Manuf. Technol. 100 3025–35
- [22] Sun W et al 2022 Establishment of x-ray computed tomography traceability for additively manufactured surface texture evaluation Addit. Manuf. 50 102558
- [23] Feldkamp L, Davis L and Kress J 1984 Practical cone-beam algorithm J. Opt. Soc. Am. A 1 612–9
- [24] Haitham Shammaa M, Ohtake Y and Suzuki H 2010 Segmentation of multi-material CT data of mechanical parts for extracting boundary surfaces Comput.-Aided Des. 42 118–28
- [25] Lifton J, Malcolm A, McBride J and Cross J 2013 The application of voxel size correction in x-ray computed tomography for dimensional metrology Singapore Int. NDT Conf. and Exhibition
- [26] Kak A and Slaney M 1988 Principles of Computerized Tomographic Imaging (Piscataway, NJ: IEEE)
- [27] Pan X, Sidky E and Vannier M 2009 Why do commercial CT scanners still employ traditional, filtered back-projection for image reconstruction? *Inverse Problems* 25 123009
- [28] Rezvani N 2012 Iterative Reconstruction Algorithms for Polyenergetic X-Ray Computerized Tomography (Canada: University of Montreal)
- [29] Biguri A et al 2020 Arbitrarily large tomography with iterative algorithms on multiple GPUs using the TIGRE toolbox J. Parallel Distrib. Comput. 146 52–63
- [30] Hestenes M and Stiefel E 1952 Methods of conjugate gradients for solving linear systems J. Res. Natl Bur. Stand. 49 409
- [31] Schorr C, Dörr L, Maisl M and Schuster T 2017 Registration of a priori information for computed laminography NDT E Int. 86 106–12
- [32] Helfen L, Myagotin A, Mikulík P, Pernot P, Voropaev A, Elyyan M, Di Michiel M, Baruchel J and Baumbach T 2011 On

- the implementation of computed laminography using synchrotron radiation *Rev. Sci. Instrum.* **82** 063702
- [33] Beck A and Teboulle M 2009 A fast iterative shrinkagethresholding algorithm for linear inverse problems SIAM J. Imaging Sci. 2 183–202
- [34] Rudin L I, Osher S and Fatemi E 1992 Nonlinear total variation based noise removal algorithms *Physica* D **60** 259–68
- [35] Lettenbauer H, Lotze A and Kunzmann S 2011 Method and device for identifying material boundaries of a test object Patent US20080089589A1
- [36] Welkenhuyzen F et al 2010 A test object for calibration and accuracy assessment in x-ray CT metrology IMEKO 10th Int. Symp. on Measurement and Quality Control
- [37] Kerckhofs G, Schrooten J, Wevers M, Van Marcke P and Van Cleynenbreugel T 2006 Standardisation and validation of micro-CT for the morphological characterisation of porous structures 9th Eur. Conf. Non-Destructive Testing (ECNDT) (Berlin, Germany)
- [38] Hiller J, Maisl M and Reindl L M 2012 Physical characterization and performance evaluation of an x-ray micro-computed tomography system for dimensional metrology applications *Meas. Sci. Technol.* 23 085404
- [39] Villarraga-Gómez H 2016 X-ray computed tomography for dimensional measurements *Digital Imaging*
- [40] Kraemer A and Lanza G 2016 Assessment of the measurement procedure for dimensional metrology with x-ray computed tomography *Proc. CIRP* 43 362–7
- [41] Welkenhuyzen F, Kiekens K, Pierlet M, Dewulf W, Bleys P, Kruth J and Voet A 2009 Industrial computer tomography for dimensional metrology: overview of influence factors and improvement strategies 4th Int. Conf. on Optical Measurement Techniques for Structures and Systems (OPTIMESS)
- [42] Warnett J M, Titarenko V, Kiraci E, Attridge A, Lionheart W R B, Withers P J and Williams M A 2016 Towards in-process x-ray CT for dimensional metrology *Meas. Sci. Technol.* 27 035401
- [43] Villarraga-Gómez H and Smith S T 2020 Effect of the number of projections on dimensional measurements with x-ray computed tomography *Precis. Eng.* **66** 445–56
- [44] Schuetz P, Jerjen I, Hoffmann J, Plamondon M, Flisch A and Sennhauser U 2014 Reducing the influence of environmental scattering in industrial computed tomography by system optimisation and correction algorithms 11th European Conf. on Non-Destructive Testing (ECNDT)
- [45] Bartscher M, Illemann J and Neuschaefer-Rube U 2016 ISO test survey on material influence in dimensional computed tomography Case Stud. Nondestr. Test. Eval. 6 79–92
- [46] Biguri A, Dosanjh M, Hancock S and Soleimani M 2016 TIGRE: a MATLAB-GPU toolbox for CBCT image reconstruction *Biomed. Phys. Eng. Express* 2 055010
- [47] JCGM 2008 Evaluation of Measurement Data—Guide to the Expression of Uncertainty in Measurement (Geneva: International Organisation for Standardization)
- [48] Mari L 2005 The problem of foundations of measurement Measurement 38 259–66
- [49] Villarraga-Gómez H, Körner L, Leach R and Smith S T 2020 Amplitude-wavelength maps for x-ray computed tomography systems *Precis. Eng.* 64 228–42